






Inhomogeneous-spin-momentum-induced orbital motion of birefringent particles in tight focusing of vector beams in optical tweezers

Ram Nandan Kumar ¹, Anand Dev Ranjan ¹, Sauvik Roy ¹, Subhasish Dutta Gupta ^{1,2,3},
Nirmalya Ghosh,^{1,*} and Ayan Banerjee ^{1,†}

¹*Department of Physical Sciences, Indian Institute of Science Education and Research Kolkata, Mohanpur 741246, West Bengal, India*

²*Department of Physics, Indian Institute of Technology Jodhpur, Jodhpur 342030, India*

³*Tata Institute of Fundamental Research, Hyderabad 500107, India*



(Received 28 April 2024; revised 30 June 2024; accepted 26 July 2024; published 12 August 2024)

Spin-orbit interaction (SOI) due to the tight focusing of light in optical tweezers has led to exciting and exotic avenues towards inducing rotation in microscopic particles. However, instances where the back action of the particles influences and modifies SOI effects so as to induce rotational motion are rarely known. Here we tightly focus a vector beam having radial/azimuthal polarization carrying no intrinsic angular momentum into a refractive index stratified medium and observe the orbital rotation of birefringent particles around the beam propagation axis. In order to validate our experimental findings, we perform numerical simulations of the governing equations. Our simulations reveal that the interaction of light with a birefringent particle gives rise to inhomogeneous spin currents near the focus, resulting in a finite spin momentum. This spin momentum combines with the canonical momentum to finally generate an origin-dependent orbital angular momentum, which is manifested in the rotation of the birefringent particles around the beam axis. Our study describes a unique modulation of the SOI of light due to its interaction with anisotropic particles that can open up new avenues for exotic and complex particle manipulation in optical tweezers.

DOI: [10.1103/PhysRevA.110.023512](https://doi.org/10.1103/PhysRevA.110.023512)

I. INTRODUCTION

Optical tweezers have facilitated both spin (about an axis fixed to the particle) [1,2] and orbital rotation (about the axis of the trapping laser beam) of trapped single or multiple particles [3]. While the spinning motion around the particle axes is due to exchange of the longitudinal or transverse spin angular momentum (S_z or S_\perp) of the beam with birefringent particles [1,2,4], the orbital motion is principally caused by tight focusing of Laguerre-Gauss (LG) or Bessel-Gauss beams carrying intrinsic OAM [5–7]. In addition, over the past couple of decades, researchers have revealed various exotic effects of the spin-orbit interaction (SOI) of light in scattering, imaging, and beam propagation through anisotropic media, as well as in the tight focusing of light [8–13]. Notably, manifestations of SOI, including orbital motion, have been observed by tightly focusing a spin-polarized (with positive or negative helicity) Gaussian beam through an RI-stratified medium to generate significant transverse momentum. This momentum even bears the signatures of the elusive Belinfante spin [14,15].

It is important to note that particles trapped using tweezers scatter a significant amount of light in the longitudinal direction (in both the backward and forward scattering directions), which has been mainly used to characterize the trap stiffness rather efficaciously [16,17]. The scattered light also leads to intriguing effects such as optical binding, which has been

shown to generate both attractive and repulsive interparticle forces that have been well studied and has been utilized for trapping of multiple particles [18]. However, to the best of our knowledge, the effects of light-matter interactions in modulating the SOI of light so as to produce dynamics in trapped particles has not been reported previously. Indeed, in terms of both conceptual understanding and practical applications, such studies are of particular importance in the case of trapped birefringent particles. This follows because scattering of tightly focused light from anisotropic birefringent particles may significantly modify the local field and polarization distributions of the incident light. In most of the previously reported studies on SOI of light due to tight focusing in optical tweezers, the role of the modified field and polarization distribution of the scattered light from trapped particles have been mostly ignored. Yet this secondary effect is expected to alter the inhomogeneous polarization distribution, which is at the heart of the effects produced by SOI, and is thus expected to render them more intricate and intriguing [8,19]. Here the choice of the state of polarization of the input light would play a crucial role too. Specifically, the choice of an inhomogeneously polarized (radial/azimuthal polarization) incident light beam is likely to accentuate the observed SOI effects even further as compared to input homogeneously polarized light.

This is indeed our focus of research in this paper. Thus, we employ structured vector beams as the input into an optical tweezers system. Since tight focusing inevitably generates a significant longitudinal field component, our expectation is that this would be likely to result in unexpected effects

*Contact author: nghosh@iiserkol.ac.in

†Contact author: ayan@iiserkol.ac.in

in the case of vector beams [1,20–22]. The vector beams we employ are first-order radially and azimuthally polarized, characterized by an intensity singularity on the beam axis, inhomogeneous polarization distribution, and unique properties of cylindrical symmetry in their polarization [7,23–26]. These properties allow them to maintain their polarization, which may then be controllably modified to control trap strength and geometry in optical tweezers by adjusting only the polarization of the trapping beam [26]. Such beams also undergo low-intensity losses under nonparaxial conditions [27,28]. Additionally, when tightly focused, radially and azimuthally polarized beams achieve a smaller and sharper focal spot size and reduced axial spread, respectively [28,29], making them ideal for high-precision and efficient applications such as optical trapping, microscopy, and laser material processing [7,30]. Understandably, the consequences of tight focusing of such beams on birefringent microparticles deserve attention [4,31,32]. Additionally, in our case, the tightly focused beam also propagates through a stratified refractive index (RI) medium before entering the trapping region inside our sample chamber [33]. The influence of the stratified medium is actually crucial in determining the interaction of the light beam with the particles and influencing their dynamics, as we had observed earlier in Refs. [15,33]. In the present scenario, for input of radially or azimuthally polarized light, the canonical momentum and the spin momentum (SM) together generate a substantial origin-dependent (extrinsic) OAM of light, which we exploit to rotate trapped birefringent particles in the transverse plane around the beam axis [34,35]. The exclusive signature of the spin momentum was apparent from the orbital motion readily induced in birefringent particles, while polystyrene microspheres (nonbirefringent) of the same diameter remained unaffected. The spin momentum appears here due to the generation of local spin currents (regions of elliptical polarization) around the beam axis as a consequence of the interaction of the inhomogeneous input polarization (having no input ellipticity) at the trap focal plane with the birefringent particles having a high value of linear retardance (phase anisotropy effect). We explain all observed experimental effects by carrying out rigorous numerical simulations of the equations governing our system for different RI values of the stratified medium that the tightly focused beam encounters. Our work provides an experimentally viable strategy for engineering optical traps with controlled and specific orbital motion of trapped particles by SOI effects generated by tight focusing alone, without the need for complex algorithms involving adaptive optics. In what follows, we first describe our experiments and observations.

II. EXPERIMENTAL RESULTS

The schematic and details of our optical tweezers setup are provided in Appendix C (see Fig. 7 there). Thus, we use a conventional optical tweezers configuration consisting of an inverted microscope (Carl Zeiss Axiovert.A1) with an oil-immersion 100 \times objective (Zeiss, NA 1.4) and a solid-state laser (Lasever, 671 nm, 350 mW) coupled to the back port of the microscope. We use a vortex half-wave retarder (q-plate) of zero order for generating structured vector beams (i.e., first-order radially and azimuthally polarized vector beams).

We fix the fast axis orientation of the vortex plate ($q = \frac{1}{2}$) in such a way that it converts linear x -polarized and y -polarized light into azimuthally and radially polarized light, respectively [8,36]. For the probe particles, we first fabricate the RM257 particles, which are optically anisotropic and birefringent. The dielectric constants ϵ_{\parallel} and ϵ_{\perp} are related to the ordinary and extraordinary refractive indices n_{\parallel} and n_{\perp} of the birefringent particle through the relationships $n_{\parallel}^2 = \epsilon_{\parallel}$ and $n_{\perp}^2 = \epsilon_{\perp}$. In the case of RM257 birefringent particles, there is an approximate difference of 0.13 between the ordinary and extraordinary refractive indices [37]. Detailed information on the fabrication procedures is available in Appendix C. Subsequently, we quantify the linear retardance (δ) of the RM257 particles by analyzing the Mueller matrix. This measured value provides valuable insights into the OAM transfer dynamics, allowing us to comprehensively probe the influence of OAM in the experimental setup. We then couple the radially (azimuthally) polarized vector beam into the microscope so that it is tightly focused into the stratified medium (the arrangement and details of the stratified medium are given in Sec. V). The cover slip and the glass slide sandwiched together comprise the sample chamber into which we add approximately 20 μl of the aqueous dispersion of the RM257 particles. The mean size of these particles is 1–3 μm with a standard deviation of 20%. We collect the forward-transmitted light from the microscope lamp, as well as back-reflected light from the RM257 particles, to characterize the orbital motion. The OAM transfer to particles trapped at the trap center is optimized by varying the z focus of the microscope objective.

The experimental results are shown in Figs. 1(a) and 1(b). We probe the effect of total OAM by trapping birefringent RM257 particles using radially and azimuthally polarized vector beams. In Fig. 1(a), we observe that a single large particle (size around 2 μm) is trapped at the beam center, while another smaller particle (size around 1.5 μm) is rotating in the clockwise direction in the annular ring in time lapsed images (see video 1 in the Supplemental Material [38]). In the case of azimuthally polarized light, RM257 particles are not trapped at the center of the beam because the longitudinal component of the electric field is zero, so we observe single particles, as well as clusters, rotating clockwise around the beam center (see video 2 in the Supplemental Material [38]). The yellow arrow in the time-lapsed images in Fig. 1(b) shows the position of the orbiting particle in the annular intensity ring. Thus, these experiments clearly demonstrate that tight focusing of radially and azimuthally polarized light generates OAM that helps in rotating the particles about the beam propagation axis, even though the beam does not contain any spin angular momentum (SAM) and intrinsic OAM. In addition, as we increase the laser power, we notice a corresponding rise in the rotation speed of the particles. This is expected, since higher input beam intensity leads to increased magnitudes of both the electric and magnetic fields.

III. ELLIPTICITY GENERATION

It is important to note that the first-order radially and azimuthally polarized vector beams inherently do not

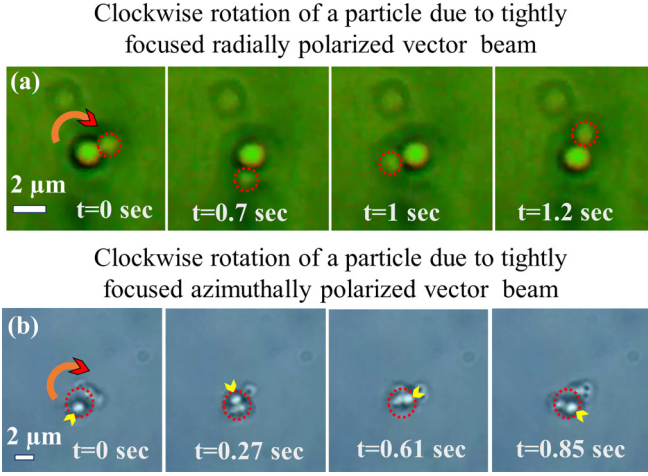


FIG. 1. Time-lapsed frames from video recordings (videos 1 and 2 in the Supplemental Material [38]) depict the rotation of particles induced by a tightly focused radially (azimuthally) polarized vector beam. (a) The trajectory of an RM257 birefringent particle rotating around another trapped particle at the center of the beam is marked by red circles, even though the two particles are at slightly different axial depths. (b) The red circle shows the orbit of rotation of similar particles at $2 \mu\text{m}$ away from the focus of the azimuthally polarized vector beam, and the yellow arrow shows the position of the orbiting particle in the red circle. It is important to note that there is zero intensity ($E_z = 0$) at the center of the beam. As a result, particles orbit solely in the annular intensity ring.

possess any SAM and OAM. However, when interacting with birefringent RM257 particles within a tightly focused beam in the stratified medium, ellipticity is induced in the output beam. To quantify this induced ellipticity, we analyze the Mueller matrix of an RM257 particle, which reveals its birefringence characteristics, as depicted in Fig. 8 in Appendix C. Figure 2(a) illustrates the spatial variation of the linear retardance (δ) of the RM257 particles. The standard Jones calculations of focused radially and azimuthally polarized vector beams on the birefringent RM257 particle are given

$$\begin{aligned} \begin{bmatrix} E_x^o \\ E_y^o \\ E_z^o \end{bmatrix}_R &= A r^{m+1} \exp(im\phi) \int_0^{\theta_{\max}} f_\omega(\theta) \cos^{3/2} \theta \sin^2 \theta \exp(ikz \cos \theta), \\ &\times \begin{bmatrix} -i[J_{m+1}(\beta) - J_{m-1}(\beta)] \cos \phi + [J_{m+1}(\beta) + J_{m-1}(\beta)] \sin \phi \\ -i[J_{m+1}(\beta) - J_{m-1}(\beta)] \sin \phi - [J_{m+1}(\beta) + J_{m-1}(\beta)] \cos \phi \\ 2 \tan \theta J_m(\beta) \end{bmatrix} d\theta. \end{aligned} \quad (3)$$

Similarly, the general form of the Cartesian components of the electric field of the azimuthally polarized vector beam can be expressed as

$$\begin{aligned} \begin{bmatrix} E_x^o \\ E_y^o \\ E_z^o \end{bmatrix}_A &= A i r^{m+1} \exp(im\phi) \int_0^{\theta_{\max}} f_\omega(\theta) \cos^{1/2} \theta \sin^2 \theta \exp(ikz \cos \theta), \\ &\times \begin{bmatrix} [J_{m+1}(\beta) + J_{m-1}(\beta)] \cos \phi + i[J_{m+1}(\beta) - J_{m-1}(\beta)] \sin \phi \\ [J_{m+1}(\beta) + J_{m-1}(\beta)] \sin \phi - i[J_{m+1}(\beta) - J_{m-1}(\beta)] \cos \phi \\ 0 \end{bmatrix} d\theta, \end{aligned} \quad (4)$$

as

$$\begin{pmatrix} 1 & 0 \\ 0 & e^{i\delta} \end{pmatrix} \begin{pmatrix} -iI_{11} \cos \phi \\ -iI_{11} \sin \phi \end{pmatrix} = \begin{pmatrix} -iI_{11} \cos \phi \\ -iI_{11} e^{i\delta} \sin \phi \end{pmatrix}_{\text{Rad}}, \quad (1)$$

$$\begin{pmatrix} 1 & 0 \\ 0 & e^{i\delta} \end{pmatrix} \begin{pmatrix} iI_{12} \sin \phi \\ -iI_{12} \cos \phi \end{pmatrix} = \begin{pmatrix} +iI_{12} \sin \phi \\ -iI_{12} e^{i\delta} \cos \phi \end{pmatrix}_{\text{Azi}}, \quad (2)$$

where δ is the linear retardance of the RM257 particles; Eqs. (1) and (2) are the resultant Jones vectors of the focused output field of radially and azimuthally polarized vector beams, respectively. We take the maximum value of the linear retardance (δ) of the RM257 particles and calculate the Stokes vectors using Eqs. (1) and (2). Using the Stokes vector analysis, we plotted the polarization ellipse of the emerging radially and azimuthally polarized field from the particles shown in Figs. 2(b) and 2(c), respectively (details of the numerical simulations of ellipticity generation are mentioned in Sec. V C). This observation leads us to the conclusion that the contribution of Belinfante's spin momentum (BSM) is also crucial in the calculation of total OAM. Consequently, it is clear that birefringent particles would be experiencing a higher total OAM compared to nonbirefringent particles such as polystyrene, thus enabling their rotation around the beam axis. We now attempt to explain our experimental observations using numerical simulations, which we perform using the theoretical formalism that we describe in the next section.

IV. THEORETICAL CALCULATIONS

Tight focusing due to objective lenses with a high NA generates a nonparaxial condition [39,40]. For the determination of electric and magnetic fields of radially and azimuthally polarized vector beams under such nonparaxial conditions, we use the angular spectrum method or vector diffraction theory provided by Richards and Wolf [6,41,42]. The general expression of Cartesian components of the electric field (E_x , E_y , and E_z) of a focused radially polarized vector beam in the focal plane is given as

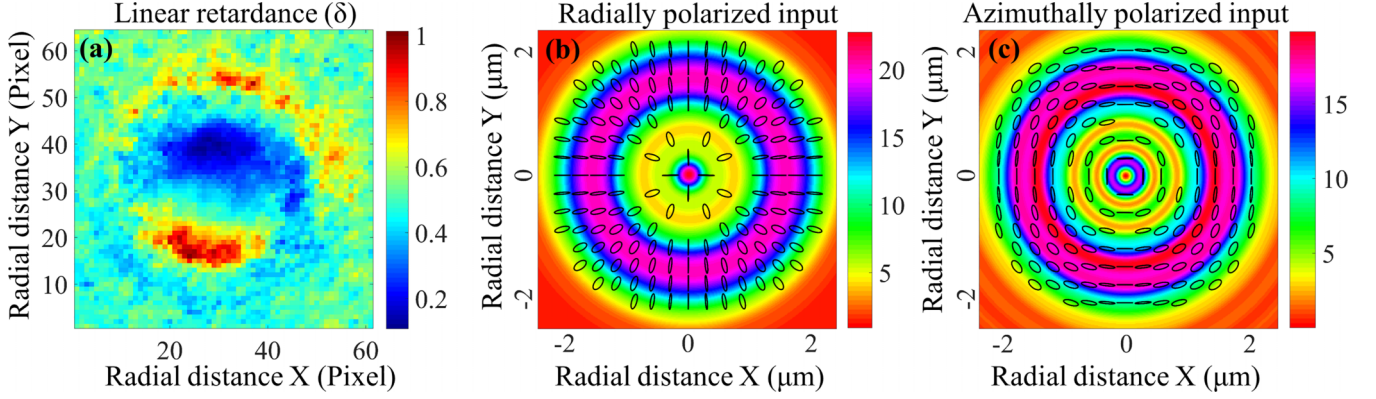


FIG. 2. (a) The linear retardance of RM257 birefringent particle. (b), (c) The polarization ellipse plots of the emerging radially and azimuthally polarized field from the RM257 birefringent particles, respectively.

where $\beta = k\rho \sin\theta$, is the argument of Bessel functions, $\theta_{\max} = \sin^{-1}(\text{NA}/n)$, which is the maximum angle related to the NA of the objective, n is the refractive index of the medium, E^o is the output electric field, A is the constant related to the amplitude of the electric field, and $f_\omega(\theta)$ is the apodization function that appears when an aplanatic lens tightly focuses the beam [40,41]. J_m is the Bessel function of m th order of the first kind, and θ and ϕ denote the polar angle with respect to the z axis and the azimuthal angle with respect to the x axis in the cylindrical (or spherical) coordinate system, respectively. Subscripts (R) and (A) of Eqs. (3) and (4) represent the radially and azimuthally polarized vector beams, respectively, and $\exp(im\phi)$ represents the helical phase, where m is the topological charge that can be any integer and $m\hbar$ is the OAM per photon. By putting $m = 0$ in Eqs. (3) and (4), we obtain the expressions of the first-order radially and azimuthally polarized vector beams [see Eqs. (A1) and (A2) in Appendix A]. For radially polarized light, the magnetic field vectors exhibit an azimuthal orientation, while for azimuthally polarized light this changes to radial [see Eqs. (A3) and (A4) in Appendix A]. Importantly, calculations of spin angular momentum (SAM) indicate that the longitudinal component of SAM (S_z) is zero for both radially and azimuthally polarized light, with only the transverse SAM (TSAM) being nonzero for both radially and azimuthally polarized vector beams as has been clearly shown in Refs. [4,31].

We now determine analytical expressions for the total OAM densities for tightly focused first-order ($m = 0$) radially and azimuthally polarized vector beams. For this, we first note that the linear momentum density \mathbf{P} for a monochromatic electromagnetic field in SI units is related to the time-averaged Poynting vector through $\mathbf{P} = \text{Re}(\mathbf{E}^* \times \mathbf{H})/(2c^2)$ [or $\mathbf{P} = \text{Re}(\mathbf{E} \times \mathbf{H}^*)/(2c^2)$] [34,43,44]. For the vector fields, we can decompose \mathbf{P} into \mathbf{P}^o , which is the canonical or orbital momentum (CM) derived from the local phase gradient (wave vector) in the field, and a Belinfante's spin momentum (BSM) \mathbf{P}^s , which arises as a consequence of spin inhomogeneity [44,45]. Therefore, we can write $\mathbf{P} = \mathbf{P}^o + \mathbf{P}^s$, where $\mathbf{P}^o = \frac{1}{4\omega m^2} \text{Im}[\epsilon \mathbf{E}^* \cdot (\nabla) \mathbf{E} + \mu \mathbf{H}^* \cdot (\nabla) \mathbf{H}]$ and $\mathbf{P}^s = \frac{1}{8\omega m^2} \nabla \times \text{Im}(\epsilon \mathbf{E}^* \times \mathbf{E} + \mu \mathbf{H}^* \times \mathbf{H})$, with ϵ being the permittivity, μ the permeability, and n the refractive index of the embedding medium. The canonical P^o (orbital) and spin P^s parts

of the momentum density generate the total OAM density of the electromagnetic field [45–47]. The total OAM density is $\mathbf{L} = \mathbf{r} \times \mathbf{P}$, where \mathbf{r} is the lateral position of the corresponding beam propagation axis [34]. Hence, the density of the linear momentum \mathbf{P} and total OAM \mathbf{L} for the radially (azimuthally) polarized vector beams on tight focusing in optical tweezers may be written as

$$\begin{aligned}
 P_x &= \text{Re}[C i(I_{12} I_{10}^*) \cos \phi], \\
 P_y &= \text{Re}[C i(I_{12} I_{10}^*) \sin \phi], \\
 P_z &= \text{Re}[C(I_{12} I_{11}^*)], \\
 L_x &= yP_z - zP_y, \\
 L_y &= zP_x - xP_z, \\
 L_z &= xP_y - yP_x.
 \end{aligned} \tag{5}$$

Here C is the constant denoting \mathbf{P} , while I_{10} , I_{11} , and I_{12} are the complex diffraction integrals detailed in Eq. (A5) in Appendix A [4,33,39,40]. Generally, Laguerre-Gaussian (LG $_{pl}$) beams [48], high-order Bessel beams [49], and Mathieu beams [50] inherently possess OAM. The mechanical action of any nonzero values of OAM ($m \neq 0$) causes particles to exhibit orbital motion around the beam propagation axis, as demonstrated in previous works [5,6,51]. However, in the case of beams with zero SAM ($\sigma = 0$) and intrinsic OAM, such as first-order ($m = 0$) radially and azimuthally polarized vector beams, birefringent particles still orbit around the beam center due to SOI effects, as we have shown. To understand our observations, we now proceed to numerically simulate our experimental system and evaluate the intensity distributions, OAM characteristics and ellipticity generation.

V. NUMERICAL SIMULATIONS

In our experimental system, the output from a high NA objective lenses in an optical tweezers setup is passed through a stratified medium. The laser beam of wavelength 671 nm is incident on the 100 \times oil immersion objective lens of NA 1.4 followed by (1) an oil layer of thickness around 5 μm and refractive index (RI) 1.516, (2) a 160 μm thick coverslip having refractive index varying between 1.516–1.814

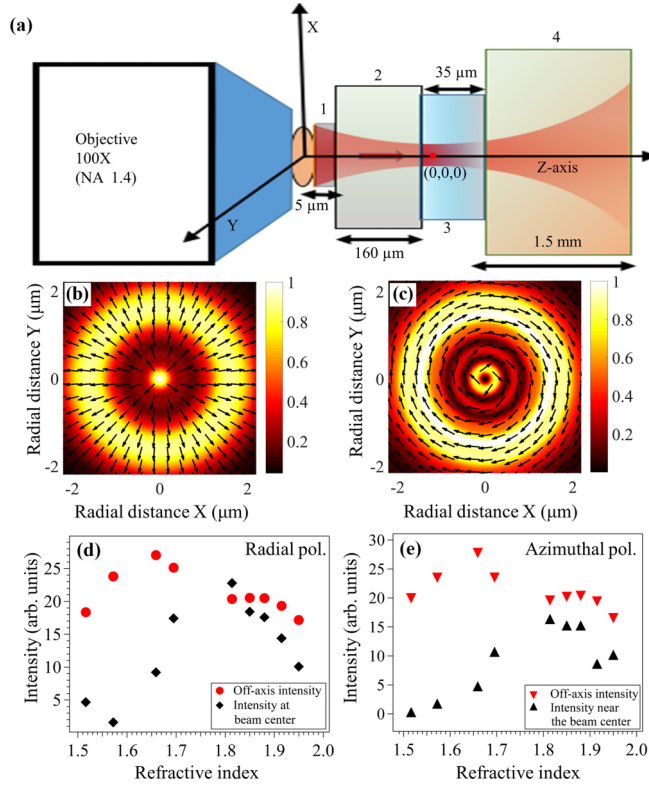


FIG. 3. (a) Schematic diagrams of the stratified medium used in our numerical analysis and in the optical tweezers system. (b)–(e) Numerical simulation of the intensity distribution at $z = 2 \mu\text{m}$ away from the focus for a mismatch RI of 1.814 using the high NA objective (trap focus) lens. (b), (c) The quiver plots over the intensity distribution depict the radial and azimuthal polarization of the vector beams, respectively. (d), (e) Comparison of intensities at the beam center (or near the beam center) denoted by solid black squares and black triangles, and the off-axis annular ring represented by solid red circles and red triangles as a function of RI for input radially and azimuthally polarized vector beams, respectively.

(note that the case where $\text{RI} = 1.516$ is henceforth referred to as the “matched condition,” which is typically employed in optical tweezers to minimize spherical aberration effects in the focused beam spot, whereas the other values are referred to as a “mismatched” condition), (3) a sample chamber of an aqueous solution of birefringent RM257 particles in a water medium having a refractive index of 1.33 with a depth of $35 \mu\text{m}$, and finally (4) a glass slide of refractive index 1.516 whose thickness we consider to be semi-infinite ($1500 \mu\text{m}$). In the simulation, the origin of coordinates is located inside the sample chamber, marked by a red circle on the z axis at an axial distance of $5 \mu\text{m}$ from the interface between the sample and the coverslip [see Fig. 3(a)]. Thus, the objective-oil interface is at $-170 \mu\text{m}$, the oil-cover slip interface is at $-165 \mu\text{m}$, and the cover slip-sample chamber interface is at $-5 \mu\text{m}$, and the sample chamber-glass slide interface is at $+30 \mu\text{m}$. At the first interface (objective lens), we perform a paraxial to nonparaxial transformation, and decompose the radial and azimuthally polarized incident ray E_{inc} into s and p polarizations, respectively. For each polarization state, we account for the corresponding Fresnel transmission coefficients T_s and T_p , as well as the

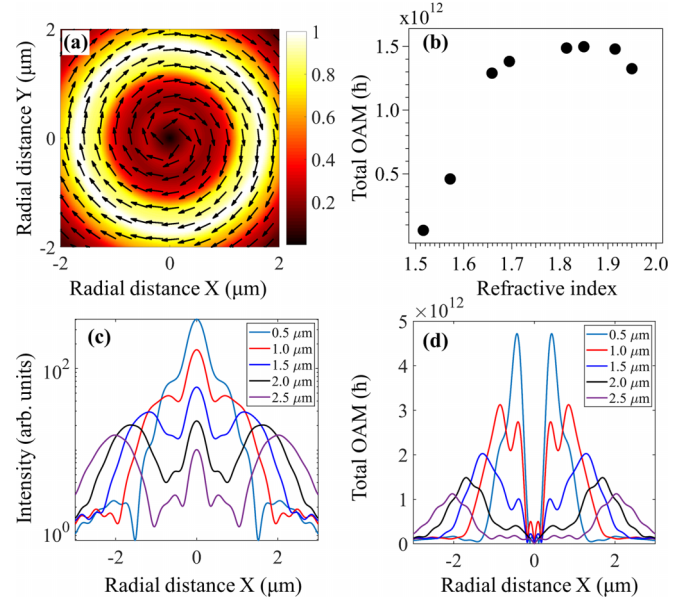


FIG. 4. (a) Quiver plot of the origin-dependent OAM at $2 \mu\text{m}$ away from the focus of a radially (azimuthally) polarized vector beam for mismatched RI (1.814). Note that the magnitude of the OAM for both beams is the same. (b) The maximum value of OAM is a function of RI. It is evident that the OAM is at its maximum at an RI of 1.814, which is consistent with our experimental conditions. Line plot of the radial intensity (in log scale) and total OAM distribution of a radially polarized beam at different z planes for mismatched RI (1.814), shown in (c) and (d), respectively.

reflection coefficients R_s and R_p at each interface of the stratified medium [39,40].

A. Numerical simulations of intensity distribution

The schematic in Fig. 3(a) provides a cartoon representation of our system. We conduct the numerical simulations to investigate the tight focusing of the input radially/azimuthally polarized vector beam by a high NA objective lens into a stratified medium under “mismatched” conditions (though the experimental observations are for the mismatched case). Consistent with the theoretical predictions, we observe that the electric field intensity at the center of a radially polarized beam is a result of I_{long} (I_{10}), while the off-axis intensity arises from I_{rad} (I_{11}), as illustrated in Figs. 3(b) and 3(d). On the contrary, for an azimuthally polarized beam, as depicted in Figs. 3(c) and 3(e), the electric field intensity near the beam center and the off-axis annular ring is formed due to I_{azi} (I_{12}). The quiver plots over the intensity distribution depict the radial and azimuthal polarization of the vector beams in Figs. 3(b) and 3(c), respectively. In addition, we quantified the radial ($|E_\rho|^2$), azimuthal ($|E_\phi|^2$), and longitudinal ($|E_z|^2$) components of the electric field and compared them separately. We found that the azimuthal component dominates at the off-axis position of the intensity distributions at $z = 2 \mu\text{m}$ away from the focus for an RI of 1.814 (see Fig. 5 in Appendix B). In the case of azimuthally polarized light, at the center of the beam, the electric field intensity is found to be zero due to the absence of the longitudinal component (E_z) of the electric

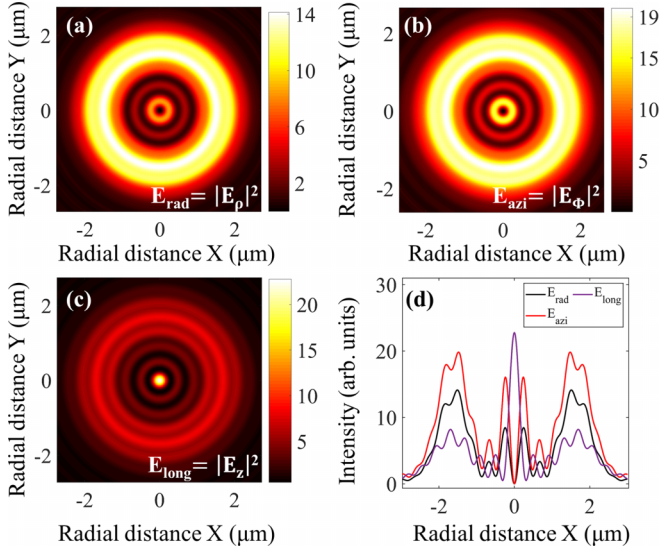


FIG. 5. (a), (b), (c) Numerical simulation of the radial, azimuthal, and longitudinal components of the electric field intensity distribution at $z = 2 \mu\text{m}$ away from the focus for a refractive index (RI) of 1.814 using the high numerical aperture (NA) objective lens, respectively. (d) Component-wise comparison of intensities at the off-axis and on-axis (beam center) positions of the intensity distribution.

field. It is evident from Figs. 3(d) and 3(e) that, for input radial (or azimuthal) polarization, the total intensity (resulting from both electric and magnetic fields) at the beam center (or near the beam center) at an axial distance of $2 \mu\text{m}$ from the focus increases as the RI contrast of the stratified medium increases up to 1.814. Beyond this point, the intensity at both the beam center (or near the beam center) and the off-axis positions decreases as a result of the transverse spread of the beam. For RI 1.814, the intensity at the beam center is approximately 10% higher than that in the annular ring for radial polarization, allowing particles to be trapped in both regions, which is what we use in our experiments.

B. Numerical simulations of OAM distribution

The results of our simulations correspond to origin-dependent total OAM are shown in Fig. 4. For OAM [Fig. 4(a)–4(d)] and the radial distribution of intensity [Fig. 4(c)], we present results for the mismatched RI 1.814. This is because the value of OAM increases as the RI of the coverslip is increased up to 1.88, as shown in Fig. 4(b). Also, the spherically aberrated intensity profile that we obtain in this case allows overlap between significant intensity and large OAM that is useful to see effects on mesoscopic particles of a diameter of a few microns [4,15]. Note that we also perform the simulations not at the focal region of the trap, but at $2 \mu\text{m}$ away from the focus, so as to obtain enough spatial extent of both intensity and OAM to obtain experimentally discernible effects. The corresponding intensity distributions as a function of axial distance from focus for the mismatched RI 1.814 are shown in Fig. 4(c) shows that as we move away from the focus, off-axis intensity lobes are formed. The quiver plot in Fig. 4(a) illustrates that the total OAM for the mismatched

RI case follows a clockwise direction and is distributed in an annular ring around the focus. We have shown that particles trapped in this ring would exhibit rotational motion around the beam center. On this note, Fig. 4(b) shows that the maximum value of the OAM distribution at $2 \mu\text{m}$ away from the focus depends on the RI. It is evident that the OAM saturates between an RI of 1.80 and 1.88. For RI values greater than 1.88, both intensity [see Figs. 3(d) and 3(e)] and OAM decrease rapidly due to the transverse spread of the beam. In our experiments, we therefore used an RI of 1.814. Fig. 4(d) demonstrates the radial distributions of total OAM as a function of axial distance from focus for the mismatched RI 1.814. From this, it follows that the OAM peaks overlap with off-axis intensity peaks [see Fig. 4(c)], suggesting that birefringent RM257 particles trapped on the off-axis would feel its effects the most.

C. Numerical simulations of ellipticity generation

The results of our simulations correspond to the generation of ellipticity in the output beam emerging from the birefringent RM257 particle, as shown in Figs. 2(b) and 2(c). We conducted the numerical simulations at $2 \mu\text{m}$ away from the focus for the “mismatched” condition of the coverslip with RI 1.814. Using the LU-Chipman (or polar) decomposition [13,52,53], we quantified the linear retardance of the RM257 particles, as shown in Fig. 2(a). From there, we took the highest value of the linear retardance of the birefringent RM257 particle and wrote a generalized 2×2 Jones matrix for the optically anisotropic medium (birefringent particle). Using the expressions for the electric field of first order radially and azimuthally polarized vector beams [having zero intrinsic SAM and OAM ($m = 0$)] [see Eqs. (A1) and (A2) in Appendix A], we calculated the resultant Jones vectors [Eqs. (1) and (2)] of the output field emerging from the birefringent RM257 particle. We then calculated the four Stokes vector elements $S_0 = |E_x|^2 + |E_y|^2$, $S_1 = |E_x|^2 - |E_y|^2$, $S_2 = 2 \text{Re}(E_x^* E_y)$, and $S_3 = 2 \text{Im}(E_x^* E_y)$ of the output beam [54,55]. Using a polarimetry MATLAB code, we plotted the polarization ellipse over the intensity distribution of radially and azimuthally polarized vector beams in Figs. 2(b) and 2(c), respectively. Hence, we concluded that the emerging vector beam from the birefringent particle has gained finite helicity (or ellipticity). Therefore, the contribution of Belinfante’s spin momentum (BSM) is also crucial in the calculation of total OAM.

VI. CONCLUSION

In conclusion, we use the SOI of light generated due to the tight focusing of structured vector beams in optical tweezers and its modification in the presence of interactions with birefringent microparticles to engineer orbital rotation in the particles. Thus, we tightly focus radially and azimuthally polarized vector beams that do not carry any SAM and intrinsic OAM into a RI-stratified medium and observe the effect of total OAM on birefringent particles orbiting around the beam propagation axis. We see clear signatures of origin-dependent OAM generated for both input polarizations. These effects are also facilitated by the spherical aberrated intensity profile

generated by our RI-stratified medium. Most importantly, the interaction of the focused light with the birefringent particles results in the generation of a finite BSM that actually enables the orbital rotation, which—importantly—is not observed in nonbirefringent particles. Consequently, our work demonstrates how light-matter interactions may modify the effects of the SOI of light in optical tweezers to generate interesting dynamics in trapped particles. Importantly, these effects arise from the SOI generated by tight focusing alone, without the need to structure complex beam profiles using advanced algorithms involving adaptive optics. In the future, we plan to observe the effects on SOI in a nonlinear medium and intend to extend our work on ENZ (Epsilon Near Zero) materials [56].

ACKNOWLEDGMENTS

The authors acknowledge the SERB, Department of Science and Technology, Government of India (Project No. EMR/2017/001456). R.N.K. acknowledges IISER Kolkata for providing an IPh.D research fellowship.

APPENDIX A: THEORETICAL CALCULATIONS

For the determination of electric and magnetic fields of radially and azimuthally polarized vector beams under such nonparaxial conditions, we use the angular spectrum method or vector diffraction theory provided by Richards and Wolf [6,41,42]. By employing $m = 0$ in Eqs. (3) and (4), we can write the expressions for the electric field components (E_x , E_y , and E_z) of first-order radially and azimuthally polarized vector beams [having zero intrinsic OAM ($m = 0$)] as [40]

$$\begin{bmatrix} E_x^0 \\ E_y^0 \\ E_z^0 \end{bmatrix}_{\text{Rad}} = A \begin{bmatrix} (-iI_{11}) \cos \phi \\ (-iI_{11}) \sin \phi \\ I_{10} \end{bmatrix}, \quad (\text{A1})$$

$$\begin{bmatrix} E_x^0 \\ E_y^0 \\ E_z^0 \end{bmatrix}_{\text{Azi}} = A \begin{bmatrix} (iI_{12}) \sin \phi \\ (-iI_{12}) \cos \phi \\ 0 \end{bmatrix}. \quad (\text{A2})$$

Here I_{11} , I_{12} , and I_{10} are the diffraction or Debye-Wolf integrals [39,40,42]. Note that I_{11} and I_{12} are the integral coefficients for the transverse electric/magnetic fields, while I_{10} is the coefficient for the longitudinal component of the electric/magnetic field for first-order radially/azimuthally polarized vector beam. Furthermore, from Eqs. (3) and (4), it is clear that a z component of the electric field emerges on tight focusing of radially polarized and azimuthally polarized vector beams for $m = 0$ and $m = 1$ order, respectively [28,35,41]. On the other hand, the output electric field for an azimuthally polarized vector beam with $m = 0$ remains purely transverse in nature at the focal plane.

The magnetic field vectors exhibit an azimuthal orientation for radially polarized light, whereas for azimuthally polarized light, the orientation changes to radial. Therefore, the magnetic field of the first-order vector beam, corresponding to a radially polarized electric field, is given:

$$\begin{bmatrix} H_x^0 \\ H_y^0 \\ H_z^0 \end{bmatrix}_{\text{Rad}} = B \begin{bmatrix} (-iI_{12}) \sin \phi \\ (iI_{12}) \cos \phi \\ 0 \end{bmatrix}. \quad (\text{A3})$$

Thus, the magnetic field is azimuthal in nature, with the z component being zero for the input radially polarized vector beam.

Now, the magnetic field of a first-order azimuthally polarized vector beam is radial in nature and is given as

$$\begin{bmatrix} H_x^0 \\ H_y^0 \\ H_z^0 \end{bmatrix}_{\text{Azi}} = B \begin{bmatrix} (-iI_{11}) \cos \phi \\ (-iI_{11}) \sin \phi \\ I_{10} \end{bmatrix}, \quad (\text{A4})$$

where H^o denotes the output magnetic field, and $B = A/Z_{\mu\epsilon}$ is the constant related to the amplitude of the focused magnetic field. A z component of the magnetic field emerges on tight focusing of an azimuthally polarized vector beam for $m = 0$. The electric field, as mentioned earlier, remains entirely transverse. The complete expressions of the diffraction or Debye-Wolf integrals used in the above equations [or in Eqs. (5) and (6)] are provided as follows:

$$\begin{aligned} I_{10}^t(\rho) &= \int_0^{\theta_{\max}} E_{\text{inc}}(\theta) \sqrt{\cos \theta} \sin^2 \theta (T_p \sin \theta_j) J_0(k_1 \rho \sin \theta) e^{ik_{jz} \cos \theta_j} d\theta, \\ I_{11}^t(\rho) &= \int_0^{\theta_{\max}} E_{\text{inc}}(\theta) \sqrt{\cos \theta} \sin^2 \theta (T_p \cos \theta_j) J_1(k_1 \rho \sin \theta) e^{ik_{jz} \cos \theta_j} d\theta, \\ I_{12}^t(\rho) &= \int_0^{\theta_{\max}} E_{\text{inc}}(\theta) \sqrt{\cos \theta} \sin^2 \theta (T_s) J_1(k_1 \rho \sin \theta) e^{ik_{jz} \cos \theta_j} d\theta, \\ I_{10}^r(\rho) &= - \int_0^{\theta_{\max}} E_{\text{inc}}(\theta) \sqrt{\cos \theta} \sin^2 \theta (R_p \sin \theta_j) J_0(k_1 \rho \sin \theta) e^{ik_{jz} \cos \theta_j} d\theta, \\ I_{11}^r(\rho) &= - \int_0^{\theta_{\max}} E_{\text{inc}}(\theta) \sqrt{\cos \theta} \sin^2 \theta (R_p \cos \theta_j) J_1(k_1 \rho \sin \theta) e^{-ik_{jz} \cos \theta_j} d\theta, \\ I_{12}^r(\rho) &= \int_0^{\theta_{\max}} E_{\text{inc}}(\theta) \sqrt{\cos \theta} \sin^2 \theta (R_s) J_1(k_1 \rho \sin \theta) e^{-ik_{jz} \cos \theta_j} d\theta. \end{aligned} \quad (\text{A5})$$

Here t and r superscripts denote the transmitted and reflected components of Debye-Wolf integrals, respectively. At the boundary of paraxial to nonparaxial transformation, we decompose the radial and azimuthal polarized incident ray E_{inc} into s polarization and p polarization, respectively. For each polarization state, we account for the corresponding Fresnel transmission coefficients T_s and T_p , as well as the reflection coefficients R_s and R_p at the interface of the stratified medium [40].

APPENDIX B: NUMERICAL SIMULATIONS

Our simulations are performed for the tight focusing of the input radial/azimuthal polarized beam by a high NA objective lens into a stratified medium as described in Sec. V. The electric field in the focal plane for radial polarization exhibits nonzero radial and longitudinal components of the electric field (\mathbf{E}_ρ and \mathbf{E}_z), and an azimuthal magnetic field component (\mathbf{H}_ϕ), while the other components of the electric (\mathbf{E}_ϕ) and magnetic (\mathbf{H}_ρ and \mathbf{H}_z) fields are zero. Conversely, an azimuthally polarized vector beam contains nonzero azimuthal components of the electric field (\mathbf{E}_ϕ) and radial and longitudinal magnetic field components (\mathbf{H}_ρ and \mathbf{H}_z), while the other components of the electric (\mathbf{E}_ρ and \mathbf{E}_z) and magnetic (\mathbf{H}_ϕ) fields are zero.

Notably, the electric and magnetic field intensity profiles for the radially and azimuthally polarized vector beams in the focal plane appear as bright spots at the center of the beam, since only the zero-order Bessel function (J_0 , embedded in I_{10}) possesses a nonvanishing value at the origin. In Figs. 5(a)–5(c), we separately plot the intensity distribution of the radial ($|E_\rho|^2$ or $|I_{11}|^2$), azimuthal ($|E_\phi|^2$ or $|I_{12}|^2$), and longitudinal ($|E_z|^2$ or $|I_{10}|^2$) components of the electric/magnetic field of the vector beam in a nonparaxial regime, which is tightly focused through a high NA objective lens into the stratified medium of the RI. The line plot in Fig. 5(d) compares these components, showing that the azimuthal component dominates over the radial component at the off-axis positions, while the longitudinal component of the electric/magnetic field is mostly concentrated on-axis (beam center).

We observe that the magnetic field intensity at the center of a radially polarized beam is zero due to the absence of the longitudinal component (H_z) of the magnetic field, while off-axis intensity comes from I_{trans} (I_{12}), as illustrated in Fig. 6(a). Conversely, the magnetic field intensity at the center of an azimuthally polarized beam arises from I_{long} (I_{10}), while off-axis (annular ring) intensity comes from I_{trans} (I_{11}), as demonstrated in Fig. 6(b). In Figs. 6(c) and 6(d), we present line plots of the corresponding magnetic field intensity of the tightly focused radially and azimuthally polarized vector beams for an RI of 1.814 at $2\ \mu\text{m}$ away from the focus, respectively. Notably, for RI 1.814, the magnetic field intensity at the beam center is approximately 12% higher than the annular ring for an azimuthally polarized input beam.

APPENDIX C: EXPERIMENTAL METHODS AND SAMPLE PREPARATION

1. Experimental method

The schematic and details of our optical tweezers setup are provided in Fig. 7. We use a conventional optical

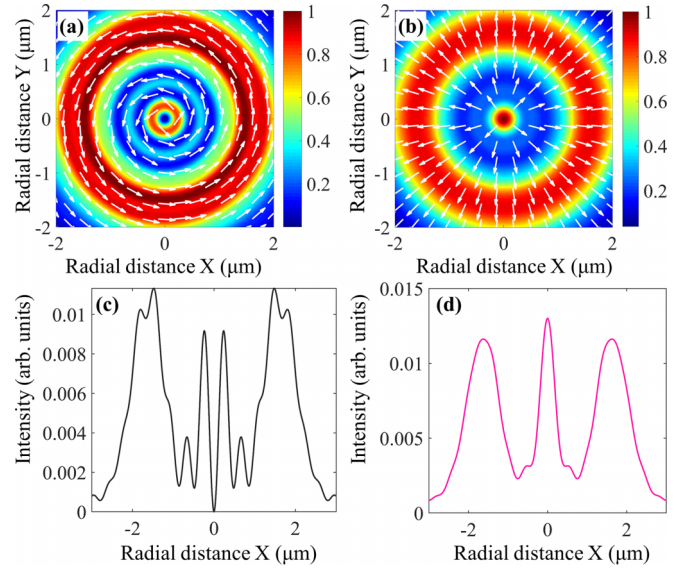


FIG. 6. Numerical simulation of the magnetic field intensity distribution at $z = 2\ \mu\text{m}$ away from the focus for a refractive index (RI) of 1.814 using the high numerical aperture (NA) objective lens. The input beams include (a) radially polarized and (b) azimuthally polarized vector beams. Line plots of the corresponding intensity distribution (xy) for the radially and azimuthally polarized vector beams under mismatched RI conditions (1.814) at $2\ \mu\text{m}$ away from the focus are presented in (c) and (d), respectively.

tweezers configuration consisting of an inverted microscope (Carl Zeiss Axiovert.A1) with an oil-immersion $100\times$ objective (Zeiss, NA 1.4), a sample chamber, and a solid-state laser (Lasever, 671 nm, 350 mW) coupled to the back port of the microscope. The sample chamber is formed by sandwiching a cover slip and a glass slide together, into which we introduce approximately $20\ \mu\text{l}$ of the aqueous dispersion of RM257. The mean size of the RM257 particles is $1\text{--}3\ \mu\text{m}$ with a standard

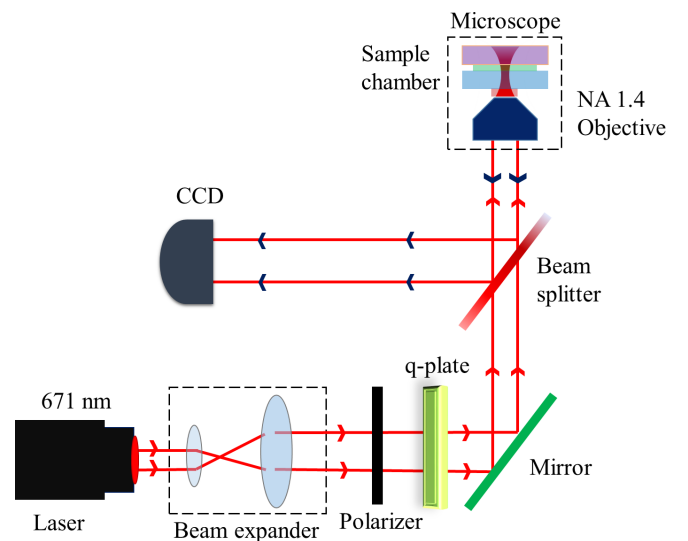


FIG. 7. Schematic representation of the experimental setup designed to couple radially or azimuthally polarized light into our optical tweezers system for conducting experiments on birefringent RM257 particles.

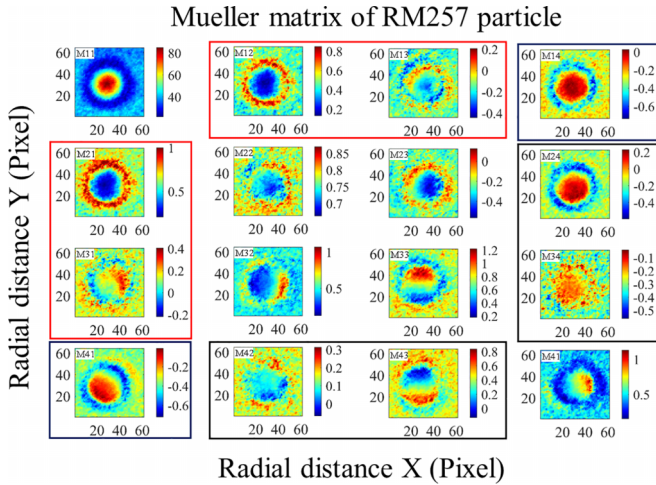


FIG. 8. The Mueller matrix of birefringent RM257 particle. Signature of linear diattenuator (elements M12, M13, M21, and M31 marked by red boxes), linear retarder (elements M24, M34, M42, and M43 marked by black boxes), and elements M14 and M41 describing the Spin-Hall effect (blue boxes) are highlighted.

deviation of 20%. To determine the Mueller matrix of RM257 particles, we employ a polarization state generator (PSG) consisting of a polarizer and a quarter-wave plate at the input of the microscope, and a polarization state analyzer (PSA) consisting of a quarter-wave plate and a polarizer at the output of the microscope. The PSG generates six different linear and circular polarization states. For this purpose, the collimated white light from the microscope's inbuilt illumination source (a 100W halogen lamp) passes through the PSG unit, which includes a rotatable linear polarizer and a quarter-wave plate corresponding to 671 nm. The light is then directed onto our sample of birefringent RM257, and the scattered light from the sample is collected by the microscope objective (Carl Zeiss Axiovert.A1, NA 1.4). Subsequently, the polarization of the scattered light is analyzed by the PSA unit, which comprises a quarter-wave plate and a linear polarizer. For each polarization state generated by the PSG, we conduct six measurements with the PSA, resulting in a total of 36 polarization-resolved projective measurements. We then construct the 4×4 Mueller matrix based on these measurements. Using the LU-Chipman (or polar) decomposition [13,52,53], we quantify the linear retardance of the RM257 particles in Fig. 2(a). Specifically, the linear retardance originates from the difference in the real part of the refractive index between two orthogonal linear polarization states. The linear retarder elements (M24, M34, M42, and M43) are highlighted by black boxes in Fig. 8.

2. Sample preparation

In the synthesis of RM257 vaterite particles, the fabrication process follows a meticulous procedure to ensure the

controlled formation of particles. The synthesis is carried out using two hot plates equipped with temperature sensors to regulate the temperature throughout the process. The following steps outline the fabrication story of RM257 birefringent particles:

Step 1: Setting up the laboratory. The experiment begins by preparing the laboratory setup with two 200 ml beakers attached to thermometers and two hot plates, each equipped with a temperature sensor. These plates are crucial for maintaining precise temperatures during synthesis.

Step 2: Solvent preparation. We took 150 ml of deionized water and 50 ml of ethanol into two different beakers, heated them separately on the hot plate to 75 °C and 55 °C, respectively, and maintained these temperatures.

Step 3: Introducing RM257. Once the ethanol reaches 55 °C, 30 mg of RM257 was added. The solution was then stirred or allowed to settle until it becomes clear again. This step ensures the proper dissolution of RM257 in ethanol.

Step 4: Controlled mixing. As the temperature of the water reaches 70 °C, the ethanol solution containing RM257 was added dropwise to the water. Care was taken to cover the mouth of the beaker containing ethanol to reduce the evaporation rate of ethanol. The controlled addition of the liquid to the water is important because it influences the size of the particles formed.

Step 5: Particle growth. To control the size of the RM257 particles, it is crucial to manage the evaporation rate of ethanol. The slower the addition of the ethanol solution, the larger the particles will be. The mixture beaker is covered with aluminum foil, and holes are made in it to reduce the evaporation rate. This step allows for the particles to grow as the ethanol gradually evaporates.

Step 6: Finalizing the synthesis. Once all the ethanol evaporated, the hot plates were switched off, and the solution was left to cool. The aluminum foil covering the beaker remained in place during this cooling period.

This fabrication process ensures the controlled synthesis of RM257 vaterite particles, whose size is influenced by careful management of temperatures and evaporation rates throughout the procedure [37]. The resulting particles are expected to exhibit birefringence characteristics. To discern the effects of birefringence characteristics of RM257 particles, we dispersed them in an aqueous solution within the sample chamber of an optical tweezers setup. The particles were then exposed to forward-transmitted light from the microscope lamp utilizing a cross-polarization scheme. This involves the strategic placement of crossed linear polarizers at both the input and output of the microscope, and we observed the intensity of the particles relative to the background. If the particles exhibit birefringence, they would scatter significant light and appear to glow when observed in the cross-polarized position.

[1] M. E. Friese, T. A. Nieminen, N. R. Heckenberg, and H. Rubinsztein-Dunlop, *Nature (London)* **394**, 348 (1998).

[2] A. B. Stilgoe, T. A. Nieminen, and H. Rubinsztein-Dunlop, *Nat. Photon.* **16**, 346 (2022).

[3] J. E. Curtis and D. G. Grier, *Phys. Rev. Lett.* **90**, 133901 (2003).

- [4] R. N. Kumar, J. K. Nayak, S. D. Gupta, N. Ghosh, and A. Banerjee, *Las. Photon. Rev.* **n/a**, 2300189 (2023).
- [5] V. Garcés-Chávez, D. McGloin, M. J. Padgett, W. Dultz, H. Schmitzer, and K. Dholakia, *Phys. Rev. Lett.* **91**, 093602 (2003).
- [6] Y. Zhao, J. S. Edgar, G. D. M. Jeffries, D. McGloin, and D. T. Chiu, *Phys. Rev. Lett.* **99**, 073901 (2007).
- [7] Q. Zhan, *Adv. Opt. Photon.* **1**, 1 (2009).
- [8] L. Marrucci, C. Manzo, and D. Paparo, *Phys. Rev. Lett.* **96**, 163905 (2006).
- [9] S. K. Ray, S. Chandel, A. K. Singh, A. Kumar, A. Mandal, S. Misra, P. Mitra, and N. Ghosh, *ACS Nano* **11**, 1641 (2017).
- [10] A. Forbes, *Laser Photonics Rev.* **13**, 1900140 (2019).
- [11] A. K. Singh, S. Saha, S. D. Gupta, and N. Ghosh, *Phys. Rev. A* **97**, 043823 (2018).
- [12] S. Fu, C. Guo, G. Liu, Y. Li, H. Yin, Z. Li, and Z. Chen, *Phys. Rev. Lett.* **123**, 243904 (2019).
- [13] J. K. Nayak, H. Suchiang, S. K. Ray, S. Guchhait, A. Banerjee, S. D. Gupta, and N. Ghosh, *Phys. Rev. Lett.* **131**, 193803 (2023).
- [14] V. V. Kotlyar, A. G. Nalimov, A. A. Kovalev, A. P. Porfirev, and S. S. Stafeev, *Phys. Rev. A* **102**, 033502 (2020).
- [15] D. Pal, S. D. Gupta, N. Ghosh, and A. Banerjee, *APL Photon.* **5**, 086106 (2020).
- [16] K. C. Neuman and S. M. Block, *Rev. Sci. Inst.* **75**, 2787 (2004).
- [17] S. B. Pal, A. Haldar, B. Roy, and A. Banerjee, *Rev. Sci. Inst.* **83**, 023108 (2012).
- [18] K. Dholakia and P. Zemánek, *Rev. Mod. Phys.* **82**, 1767 (2010).
- [19] L. Marrucci, E. Karimi, S. Slussarenko, B. Piccirillo, E. Santamato, E. Nagali, and F. Sciarrino, *Mol. Cryst. Liq. Cryst.* **561**, 48 (2012).
- [20] Y. Yang, Y.-X. Ren, M. Chen, Y. Arita, and C. Rosales-Guzmán, *Adv. Photonics* **3**, 034001 (2021).
- [21] R. N. Kumar, G. Verma, S. D. Gupta, N. Ghosh, and A. Banerjee, [arXiv:2407.16501](https://arxiv.org/abs/2407.16501).
- [22] A. Forbes, M. de Oliveira, and M. R. Dennis, *Nat. Photon.* **15**, 253 (2021).
- [23] G. Machavariani, Y. Lumer, I. Moshe, A. Meir, and S. Jackel, *Opt. Lett.* **32**, 1468 (2007).
- [24] D. L. Andrews and M. Babiker, *The Angular Momentum of Light* (Cambridge University Press, Cambridge, 2012).
- [25] K. Huang, P. Shi, G. Cao, K. Li, X. Zhang, and Y. Li, *Opt. Lett.* **36**, 888 (2011).
- [26] S. Skelton, M. Sergides, R. Saija, M. Iati, O. Maragó, and P. Jones, *Opt. Lett.* **38**, 28 (2013).
- [27] O. G. Rodríguez-Herrera, D. Lara, K. Y. Bliokh, E. A. Ostrovskaya, and C. Dainty, *Phys. Rev. Lett.* **104**, 253601 (2010).
- [28] R. Dorn, S. Quabis, and G. Leuchs, *Phys. Rev. Lett.* **91**, 233901 (2003).
- [29] Q. Zhan and J. R. Leger, *Opt. Express* **10**, 324 (2002).
- [30] D. Deng, *JOSA B* **23**, 1228 (2006).
- [31] M. Neugebauer, T. Bauer, A. Aiello, and P. Banzer, *Phys. Rev. Lett.* **114**, 063901 (2015).
- [32] K. S. Youngworth and T. G. Brown, *Opt. Express* **7**, 77 (2000).
- [33] B. Roy, N. Ghosh, S. D. Gupta, P. K. Panigrahi, S. Roy, and A. Banerjee, *Phys. Rev. A* **87**, 043823 (2013).
- [34] A. T. O’Neil, I. MacVicar, L. Allen, and M. J. Padgett, *Phys. Rev. Lett.* **88**, 053601 (2002).
- [35] L. Novotny, M. R. Beversluis, K. S. Youngworth, and T. G. Brown, *Phys. Rev. Lett.* **86**, 5251 (2001).
- [36] L. Yan, P. Gregg, E. Karimi, A. Rubano, L. Marrucci, R. Boyd, and S. Ramachandran, *Optica* **2**, 900 (2015).
- [37] K. Sandomirski, S. Martin, G. Maret, H. Stark, and T. Gisler, *J. Phys.: Condens. Matter* **16**, S4137 (2004).
- [38] See Supplemental Material at <http://link.aps.org/supplemental/10.1103/PhysRevA.110.023512> for video 1, orbital rotation of a single birefringent particle with input radial polarization, where there is another particle trapped at the beam center and video 2, orbital rotation of a cluster of birefringent particles with input azimuthal polarization.
- [39] R. N. Kumar, Yatish, S. D. Gupta, N. Ghosh, and A. Banerjee, *Phys. Rev. A* **105**, 023503 (2022).
- [40] L. Novotny and B. Hecht, *Principles of Nano-optics* (Cambridge University Press, Cambridge, 2012).
- [41] S. Sato and Y. Kozawa, *J. Opt. Soc. Am. A* **26**, 142 (2009).
- [42] B. Richards and E. Wolf, *Proc. R. Soc. London A* **253**, 358 (1959).
- [43] O. Emile and J. Emile, *Ann. Phys.* **530**, 1800111 (2018).
- [44] X. Xu and M. Nieto-Vesperinas, *Phys. Rev. Lett.* **123**, 233902 (2019).
- [45] K. Y. Bliokh, A. Y. Bekshaev, and F. Nori, *Nat. Commun.* **5**, 3300 (2014).
- [46] F. J. Belinfante, *Physica* **7**, 449 (1940).
- [47] D. E. Soper, *Classical Field Theory* (Dover Publications, New York, 2008).
- [48] A. M. Yao and M. J. Padgett, *Adv. Opt. Photon.* **3**, 161 (2011).
- [49] J. Durnin, J. J. Miceli, Jr., and J. H. Eberly, *Phys. Rev. Lett.* **58**, 1499 (1987).
- [50] J. C. Gutiérrez-Vega, M. Iturbe-Castillo, and S. Chávez-Cerda, *Opt. Lett.* **25**, 1493 (2000).
- [51] H. He, M. E. J. Friese, N. R. Heckenberg, and H. Rubinsztein-Dunlop, *Phys. Rev. Lett.* **75**, 826 (1995).
- [52] Z.-F. Xing, *J. Mod. Opt.* **39**, 461 (1992).
- [53] S.-Y. Lu and R. A. Chipman, *J. Opt. Soc. Am. A* **13**, 1106 (1996).
- [54] E. Brasselet, N. Murazawa, H. Misawa, and S. Juodkazis, *Phys. Rev. Lett.* **103**, 103903 (2009).
- [55] S. D. Gupta, N. Ghosh, and A. Banerjee, *Wave Optics: Basic Concepts and Contemporary Trends* (CRC Press, Boca Raton, FL, 2015).
- [56] J. S. Eismann, L. Ackermann, B. Kantor, S. Nechayev, M. Z. Alam, R. Fickler, R. W. Boyd, and P. Banzer, *Optica* **9**, 1094 (2022).